

Research Paper

Combining high power laser modules with compound parabolic concentrators to test components at high heat fluxes

Zachary Jackson^{*}, Alexander Bebb, Peter Ireland, Jack Nicholas

Oxford Thermofluids Institute, University of Oxford, Oxford, OX2 0ES, United Kingdom

ARTICLE INFO

Keywords:

High heat flux testing

Laser

Compound parabolic concentrator

ABSTRACT

Assessing the performance and lifetime of components is a key step towards deploying new technologies in the aerospace and fusion sectors. Experimental testing at representative thermal conditions is particularly important when investigating novel materials that have yet to be fully characterized. This paper presents the key features of a new high-power laser facility developed to test components destined for extreme environments.

This facility, OLAHF (Oxford LAsER Heating Facility), provides a maximum power of 24 kW over an area of 200 mm by 104 mm for a base intensity of 1.15 MW/m² via a combination of laser modules. A bespoke control system manages the laser and instrumentation systems as well as supporting cooling air and water infrastructure. A numerical model of the lasers is validated against supplier data, enabling high fidelity computational representation of experimental setups.

Compound parabolic concentrators (CPCs) are investigated to increase applied laser power over smaller testing surfaces. A laser module-CPC system assessed the performance of gold and aluminum coatings at a range of surfaces roughnesses. High transmission efficiencies were demonstrated when surfaces are gold coated and below 0.1 μm average roughness. Future plans for OLAHF are additionally presented, including additional test campaigns using higher power CPC systems.

1. Introduction

Technologies in the aerospace and energy sectors require engineered components to survive ever more extreme conditions. Thermal intensities of between 1 and 5 MW/m² are common in power electronics and the hot stage of gas turbines [1,2], while heat fluxes of 10 to 20 MW/m² and beyond are present in hypersonic flight, atmospheric re-entry, rocket nozzles and fusion reactors [3–5]. Components destined for these environments can meet these ever increasing demands through the deployment of state-of-the-art materials, cooling architectures, or through a combination of both.

Component longevity, which is a function of a range of static and cyclic loading conditions, is an important factor in assessing the viability of new designs. Thermal effects rising from temperature gradients and magnitude, along with thermal expansion are often the limiting operational constraints in components designed for high power systems [6–8]. It is important to quantify these effects from both the

perspective of part survivability—can the component handle the peak load?—and longevity—what is the component's useful life? Placing components directly into a full-scale test is not practical as any unexpected failures during operation risk damaging the equipment and the safety of personnel. Test facilities are therefore required to replicate the thermal conditions present in such systems to

1. Enable the investigation and verification of initial design conditions;
2. Validate the thermal behavior of component cooling system designs;
3. Limit uncertainties in the target lifespan.

The difficult task of recreating, in an experimental setting, the high temperatures and heat flux characteristic of a jet turbine or fusion reactor has been achieved at facilities of various scales, from coupon to full scale-mock up. A summary of current facilities is given in Table 1.

^{*} Corresponding author.

E-mail address: zachary.jackson@eng.ox.ac.uk (Z. Jackson).

<https://doi.org/10.1016/j.applthermaleng.2024.123383>

Received 12 February 2024; Received in revised form 11 April 2024; Accepted 8 May 2024

Available online 11 May 2024

1359-4311/© 2024 The Author(s). Published by Elsevier Ltd. This is an open access article under the CC BY license (<http://creativecommons.org/licenses/by/4.0/>).

Nomenclature

Variables			Subscript	
a	2-D aperture length	m	acc	acceptance
A	area	m ²	ci	cooling inlet
C	concentration ratio	–	CPC	compound parabolic concentrator
E	elastic modulus	Pa	exp	experiment
h	heat transfer coefficient	W/m ² K	FE	finite element
H	height	m	in	inlet
I	emission intensity	W/sr	max	maximum
k	thermal conductivity	W/mK	meas	measured
L	length	m	out	outlet
R	surface roughness	μm		
t	time	s		
T	temperature	°C		
q	heat flux	W/m ²		
Q	power	W		
Greek symbols				
α	absorption	–		
β	expansion coefficient	1/K		
η	efficiency	–		
θ	angle	radian		
ψ	emission angle	degree		
ρ_e	reflectivity	–		
σ	stress	Pa		

Methods for generating these conditions can be broadly grouped into four groups: particle beams (e.g. electron), radiative (e.g. laser), electrically-driven (e.g. induction), or convective (e.g. high temperature gas). Each has its own combination of benefits and drawbacks. Particle beam systems, for example, are capable of applying very high, well characterized powers only to electrically conductive materials (e.g. metals) in a vacuum environment. Electrically-driven methods also require conductive components. High temperature gasses allow for a wide range of component materials to be investigated but suffer from

relatively lower applied heat fluxes, significant supporting infrastructure requirements with high operating costs, and very limited spatial control of the applied energy.

Laser systems, in contrast, enable high intensity, high temperature experimentation that is not limited to conductive materials. Where the optical transmission path remains unobstructed there are no limits on the testing environment, enabling the investigation of open loop cooling designs or the protection of specialized coatings via the introduction of an inert atmosphere. Laser systems also afford a high degree of spatial and temporal control.

Despite a significant amount of investment in transitioning the next generation of materials for the fusion and aerospace industries away from exotic metal alloys and towards novel ceramic materials (e.g. ceramic matrix composites (CMCs) [25]), there remains a lack of experimental facilities with the capabilities to test components manufactured from them at representative thermal conditions. This paper is the first detailing the Oxford LAser Heating Facility (OLAHF), which was constructed to meet the testing demands imposed by these new materials and is currently the only facility in the UK with this capability. A high-level comparison placing OLAHF within the wider scope of these systems is given in Fig. 1.

The operating principles underpinning the facility are demonstrated via the one-dimensional (1-D) heat equation in Section 1.1. Facility details are then given in Section 2. This is followed by an introduction and analysis of an effort to increase the applied thermal intensity of the facility via compound parabolic concentrators (CPCs) in Section 2.3 and Section 3. Data are presented showing the successful application of heat fluxes of up to 5 MW/m² on target plates with a high level of optical transmission efficiency. A summary of up-to-date facility capabilities and next development steps is given in Sections 5 and 6.

1.1. Analytical theory: a 1-D representation

Replicating the temperature stress fields that are present in a component exposed to large thermal loads are primary aims of high temperature and high heat flux experimentation. A simplified, one-dimensional (1-D) analysis of such a component with constant material

Table 1
Facilities with the capability to generate high heat fluxes for experimental testing.

Facility	Location	Method	Power (kW)	Peak intensity (MW/m ²)	Max target area (cm ²)
<i>Particle Beam</i>					
JUDITH II [9]	FZ Juelich, DE	e [−]	200	10e ³	2500
JEBIS [10]	JAEA, JP	e [−]	400	2e ³	1800
FE200 [11]	CEA, FR	e [−]	400	60e ³	10 000
EB1200 [12]	Sandia, US	e [−]	1200	10e ³	2700
ACT2 [13]	NIFS, JP	e [−]	300	20	400
EBTH [14]	Kyushu Univ, JP	e [−]	3	35	0.5
KoHLT-EB [15]	KAERI, KO	e [−]	300	10e ³	3500
EMS-60 [16]	SWIP, PRC	e [−]	60	10e ³	100
HELCZA [17]	CVR, CZ	e [−]	800	40e ³	18 000
GLADIS [18]	IPP, DE	He ⁺ , H ⁺	2200	45	40
HEFT [19]	ASIPP, PRC	e [−]	100	10	400
<i>Radiative</i>					
HHFT [20]	Oak Ridge, USA	IR	270	6	10
CHIMERA [21]	UKAEA, UK	IR	100	20	15
OLAHF [this paper]	Oxford Univ, UK	IR	24	34	10
<i>Electrical Resistive</i>					
HIVE [22]	UKAEA, UK	Induction	45	15	30
<i>Convective</i>					
HGTR [23]	TU Dresden, DE	Hot gas	1250 °C	–	900
OPG1 [24]	Oxford Univ, UK	Plasma torch	gas temperature 21.5	4.3	7

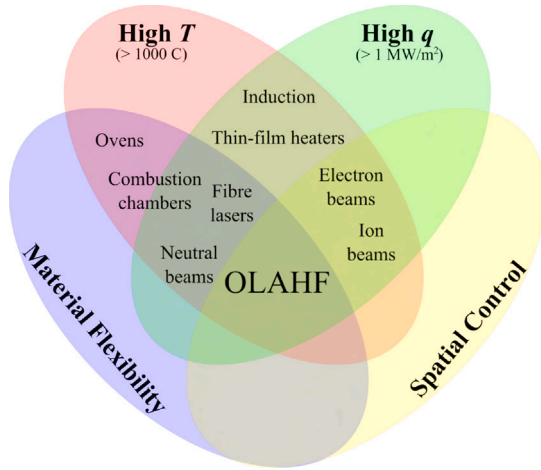


Fig. 1. A qualitative comparison of various experimental heat sources.

properties and characteristic component length L (see Appendix) reveals via Fourier's Law that the temperature gradient through this component ΔT is a function of L , the applied heat flux q , and component thermal conductivity k :

$$\Delta T = \frac{qL}{k} \quad (1)$$

The stress σ imposed on the component resulting from this temperature differential can then be related to the thermal load via a thermal loading factor [26]:

$$\frac{\sigma}{E\beta\Delta T} = \frac{\sigma}{q} \left[\frac{k}{E\beta L} \right] \quad (2)$$

where E is the elastic modulus and β is the thermal expansion coefficient.

The maximum component surface temperature T_{max} , and the resulting temperature field, can also be solved for using an expansion of the 1-D case above. Noting any cooling applied to the component during testing, represented using the Biot number Bi based on the cooling heat transfer coefficient, and assuming radiation effects are negligible, the value of T_{max} is given through the following relationships:

$$Bi = \frac{hL}{k} \quad (3)$$

$$T_{max} = \left(\frac{1 + Bi}{Bi} \right) \Delta T + T_{ci} \quad (4)$$

where T_{ci} is the coolant temperature.

The operating principals of the facility are governed by the relationships between q , ΔT , T_{max} , and σ given in Eqs. (1)–(4): laser and cooling boundary conditions can be independently controlled and set to give desirable levels of stress and component temperature.

This is demonstrated in Fig. 2 for a theoretical 5 mm thick sample made of CMSX-4 ($k \approx 20$ W/mK), a common material found in gas turbines, cooled by ambient air. Thermal constraints arise as Bi gets large and may necessitate trade-offs when fixing test conditions. For example, it may not be possible to provide a desired thermal gradient, and therefore stress, if it pushes a component above a maximum temperature.

2. Experimental facility

The following section briefly details the main facility components and support systems, which are noted in a schematic in Fig. 3. A numerical (ray tracing) model of OLAHF's laser modules is then validated against experimental data for use in further analyses.

Table 2

Input and output data acquisition modules installed at OLAHF.

Module	Type	No. channels
NI-9269	± 10 V output	4
NI-9265	20 mA output	4
NI-9474	24 V digital output	4
NI-9208	20 mA input	8
NI-9201	10 V input	8
NI-9213	Thermocouple input	2×16

2.1. OLAHF overview

OLAHF is subdivided into a Class 4 laser laboratory space and adjoining control room. The laser lab contains the main experimental space – a 1.2 m by 1.2 m (1.44 m²) optical table with vibration dampening and M6 threaded holes at regular 25 mm spacing – as well as access points to the supporting infrastructure. In addition to the separate laser support system, this is comprised of

- Chilled water, at a maximum continuous flow rate of 120 LPM and minimum temperature of 6 °C;
- Pressurized air (100 psi/6.9 bar), at a maximum continuous flow rate of 1250 SLPM at ambient conditions.
- Air extraction via HEPA filter up to 300 m³/h and maximum temperature of 300 °C.

Facility wide control is maintained via a LabVIEW-architecture system developed by AMH Test Systems¹ that integrates the majority of the facility's infrastructure and can be run in either cyclic or monotonic testing configurations. This captures the input and output signals generated during experimental testing and which are routed via a National Instruments (NI) system² installed with the modules listed in Table 2. This includes signals generated by the facility's thermal and flow instrumentation:

- **Thermal:** $2 \times$ Longwave infrared (IR) cameras³; $2 \times$ Two-color pyrometers.⁴
- **Liquid flow:** $3 \times$ Variable area flow meters.⁵
- **Air flow:** $3 \times$ Mass flow controllers.⁶

OLAHF employs seven Vertical Cavity Surface Emitting Laser (VCSEL) modules⁷ of two characteristic power levels: four, 2.4 kW and three, 4.8 kW modules for a total available power output of 24 kW. These modules are comprised of several thousand individual, micro-scale VCSEL diodes close-packed and integrated into chips. Groups of chips are combined into independent, electrically controlled emitters and integrated into a final module that supplies coolant, power and a protective air purge. This architecture is shown in Fig. 4 with module characteristics given in Table 3.

2.2. A computational VCSEL model

An accurate numerical representation of the applied laser heat flux is crucial for use in simulation work (e.g. finite element modeling) that often accompanies experimental campaigns. The apparent power of OLAHF's VCSEL modules is the summation of the incident power from thousands of individual laser diodes. Modeling the contribution from each diode is computationally expensive and requires bespoke

¹ <http://www.amhtestsystems.co.uk/>

² CompactDAQ (cDAQ-1989); <https://www.ni.com/>

³ Optris PI-640i; <https://www.optris.com/en/>

⁴ Optris CTratio 2MH; <https://www.optris.com/en/>

⁵ Omega FLMW-series; <https://www.omega.co.uk/>

⁶ ALICAT MC-series; <https://www.alicat.com/>

⁷ Trumpf Photonic Components; <https://www.trumpf.com/>

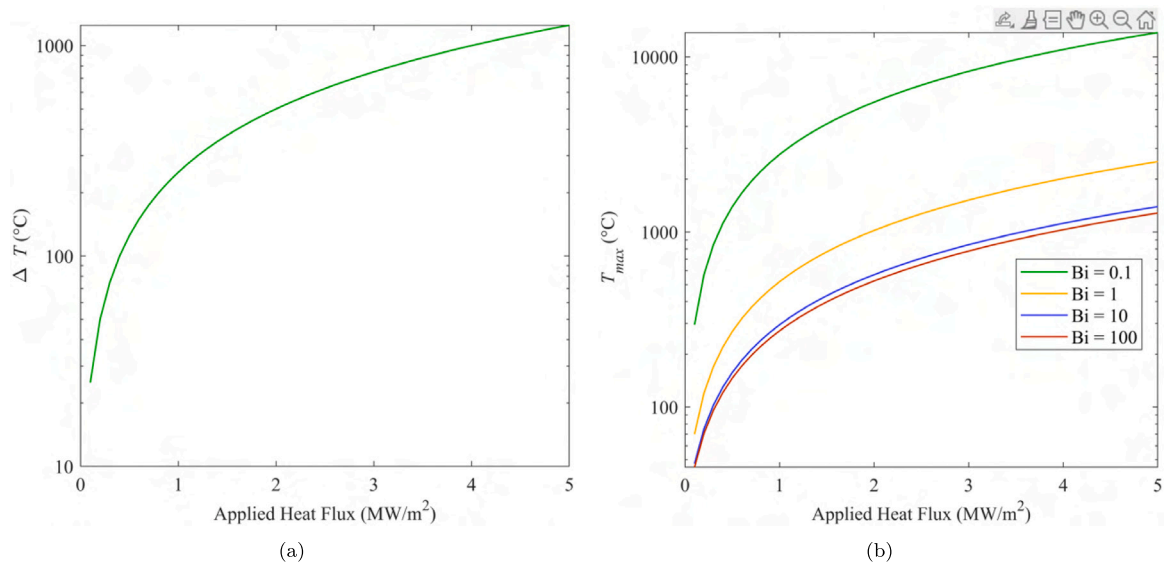


Fig. 2. Through-thickness temperature difference (a) and maximum surface temperature (b) as a function of applied laser heat flux and Biot number for a 5 mm thick sample of CMSX-4.

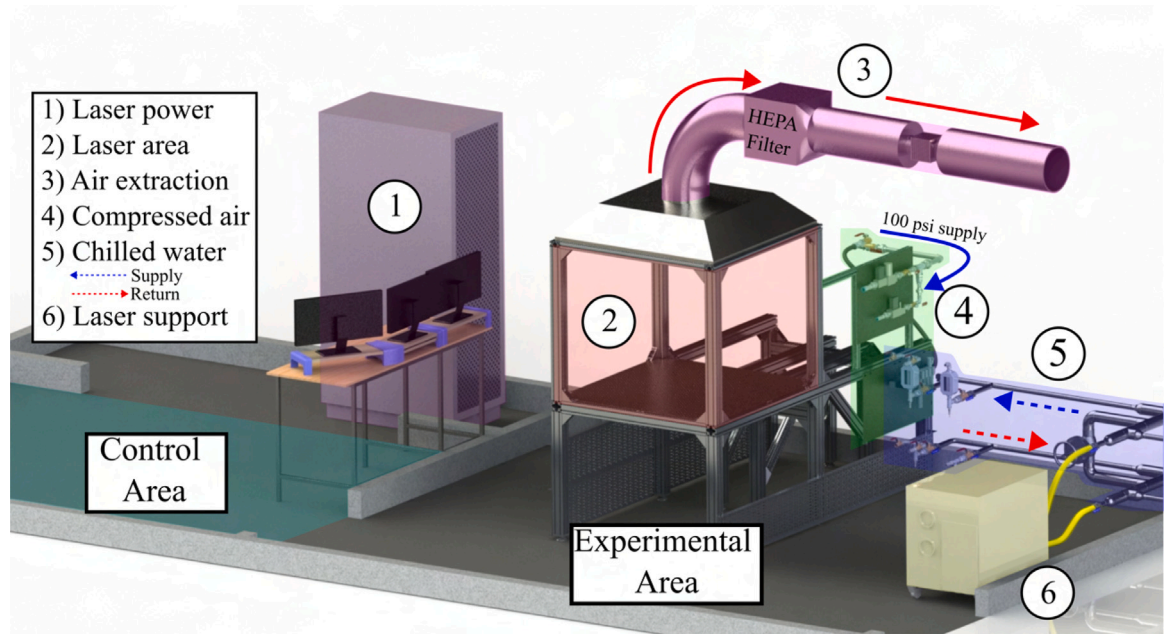


Fig. 3. Schematic of the Oxford Laser Heating Facility (OLAHF).

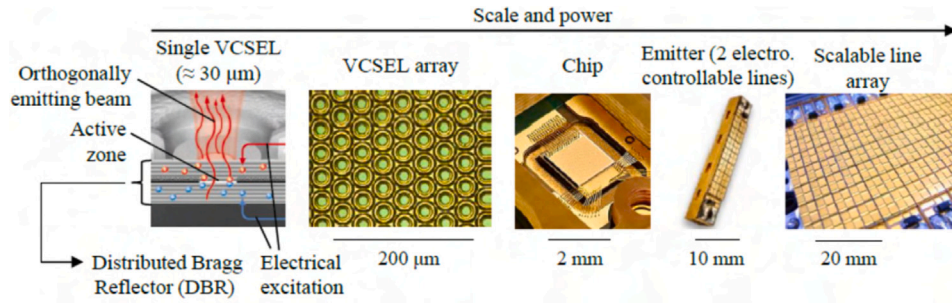
Table 3
Characteristics of the OLAHF VCSEL modules [28].

Laser module	PPM412-12-980	PPM412-24-980
Module dimensions L × W × H (mm)	107.5 × 87 × 77	159.7 × 87 × 77
Nominal optical power (kW)	2.4	4.8
Controllable zones	12	24
Emission area (mm)	40 × 52	40 × 104
Power intensity (MW/m²)	1.15 (at emission aperture)	
Wavelength (nm)	980 ± 20	
Beam half-angle (degree)	10 (for 95% power)	

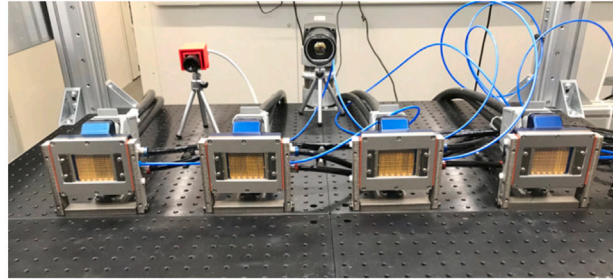
numerical analysis [27]. This study investigates the use of commercial ray tracing software as a means of creating an accurate representation of the laser module emission.

This analysis was performed using LightTools®, which employs a Monte Carlo method to simulate beam paths. Each module was simplified by consolidating the laser output into a single region corresponding to its controllable zone within each emitter. The output of these regions was then simulated at full power over a range of beam half-angles and distances from emitter-to-target surface (“offset” distance) to determine the ray tracing parameters that best characterize the laser module emission via a comparison with experimental data provided by the module supplier. It was assumed in this analysis that 100% of the incident laser was absorbed into the target.

The results of these simulations are plotted against supplier-provided experimental data in Fig. 5 at offset distances of 20, 40, and 70 mm and beam half-angles from 5 to 11 degrees. Predictably, the variation in intensity distributions increases with offset distance as differences in beam half-angle lead to more beam dispersion at larger distances. The same effect leads to the relatively small differences in intensity

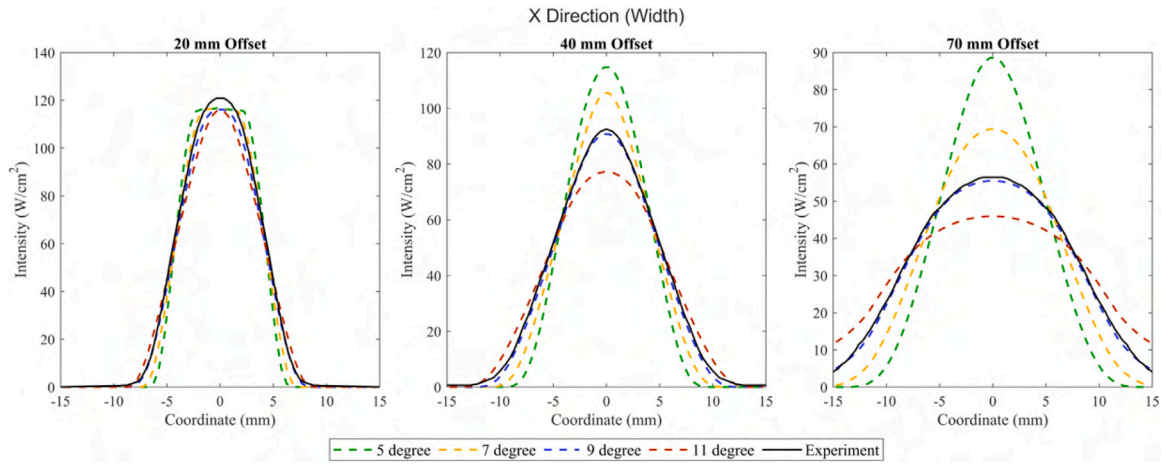


(a)

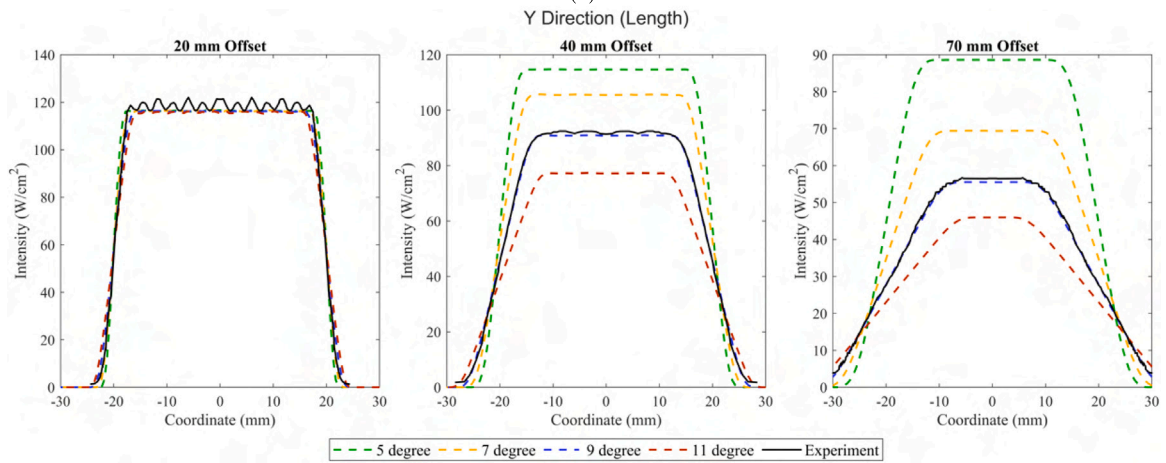


(b)

Fig. 4. VCSEL module architecture, reproduced from [27] (a), and OLAHF's four 2.4 kW modules (b).



(a)



(b)

Fig. 5. Ray-tracing predicted and experimental intensity distributions plotted across the width (a) and length (b) of a VCSEL emitter.

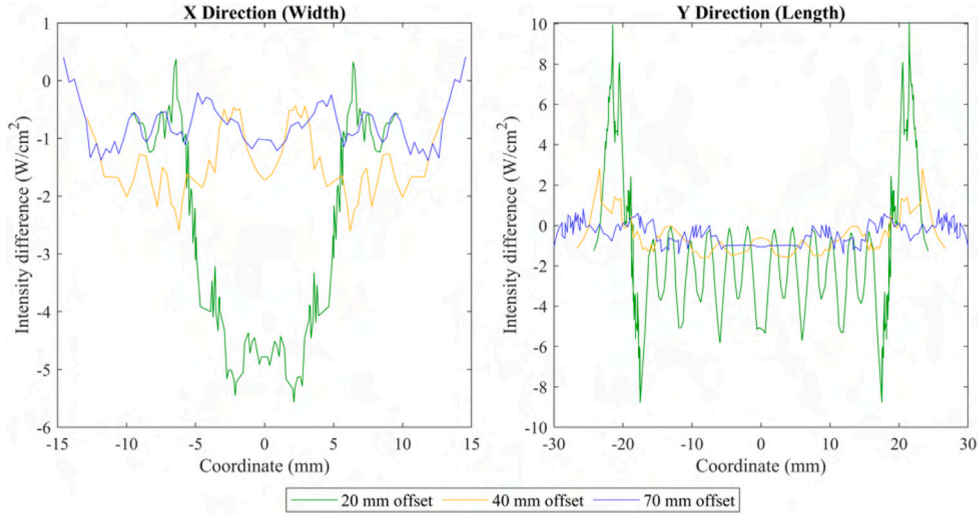


Fig. 6. Difference in ray-tracing predicted and experimental laser intensity distribution along the width (left) and length (right) of a single VCSEL emitter for a beam half-angle of 9 degrees.

Table 4
Average variation between simulated and experimental VCSEL module intensity.

Offset (mm)	Average variation (W/cm ²)	
	X direction	Y direction
20	2.61	3.32
40	1.41	0.954
70	0.782	0.526

distribution seem in the X and Y directions at the shortest offset distance of 20 mm, where smaller beam half-angles lead to a tighter intensity distribution more like a top hat than a Gaussian.

The distinctive feature at the 20 mm offset is the emergence of localized peaks along the length of the emitter. These peaks represent the individual contributions of the chips arrayed along the length of the emitter (see Fig. 4), which are not individually modeled in the ray tracing representation of the emitter. This effect is slightly visible in the 40 mm offset case. Excellent agreement is seen between the ray-tracing predicted and experimental intensity distributions in both directions along the emitter when using the 9 degree half-angle, particularly at the larger offset distances (40 and 70 mm).

Differences between predicted and experimental intensity distributions for a 9 degree half-angle approximation of the emitter are plotted in Fig. 6, with average differences given in Table 4. The simulation distributions slightly under predict the peak intensity along the width of the emitter across all offsets, and only in the center of the emission along the length. The average variation decreases as distance increases and is overall a small fraction of the maximum intensity – 2.16%, 1.52%, and 1.38% in the X direction, 2.72%, 1.03%, 0.93% in the Y direction as offsets increase from 20 mm to 70 mm, respectively – while the largest differences are confined to the edges of the emitter. Overall, these differences are suitably low and these model parameters will be carried forward to subsequent analyses.

2.3. Compound parabolic concentrators

Concentrators, in their simplest form, are non-imaging optical systems that emit radiation through a smaller aperture than first collected. The lack of an image-forming constraint allows for relatively high concentration factors and greater optical efficiencies when compared to image-forming systems [29]. A broad range of non-imaging concentrators have been developed and are widely used in industrial settings, particularly in the solar industry [30] due to their compact

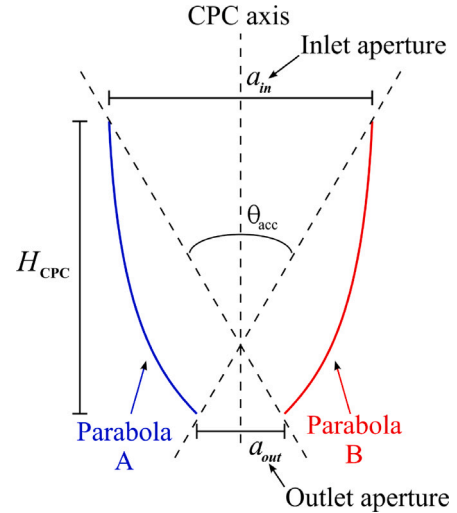


Fig. 7. 2-D CPC profile showing relevant geometric properties.

size and high efficiency. Compound parabolic concentrators (CPCs) are preferred to alternative low-concentration devices given their greater optical efficiency when concentrating both direct and diffuse light sources.

A CPC consists of mirrored parabolic faces rotated such that the focus of each is the exit point of the other as is illustrated in Fig. 7. The exact shape is obtained through a surface optimization of a light cone, a simple straight-sided concentrator, using the edge-ray principle. The coordinates for one side of a 2-D CPC are given by:

$$\begin{cases} x_{CPC} = a_{out} \cos(\theta_{CPC} + \theta_{acc}) \frac{1 + \sin \theta_{acc}}{\sin^2(\frac{\theta_{CPC}}{2})} \\ z_{CPC} = a_{out} \frac{1 - \cos(\theta_{CPC} + 2\theta_{acc}) + 2\sin(\theta_{CPC} + \theta_{acc})}{\cos(\theta_{CPC}) - 1} \end{cases} \quad (5)$$

for:

$$\frac{3\pi}{2} - \theta_{acc} \leq \theta_{CPC} \leq 2(\pi - \theta_{acc}) \quad (6)$$

The acceptance half-angle θ_{acc} is the upper limit of incident rays transmitted through the device, where any ray at or below this is transmitted while those greater are reflected and rejected. The acceptance

angle is also related to the overall height of the CPC via:

$$H_{\text{CPC}} = a_{\text{in}} \frac{1 + \sin\theta_{\text{acc}}}{2\tan\theta_{\text{acc}}} \quad (7)$$

where a_{in} is inlet aperture length. Expanding this analysis to three dimensional CPCs, which can be constructed using multiple parabolic surfaces to create a polygonal cross section, the concentration ratio C is defined as

$$C = \frac{1}{\sin^2\theta_{\text{acc}}} \quad (8)$$

The low emission half-angle characteristic of OLAHF's VCSEL modules ($\theta_{\text{acc}} \sim 9$ degrees) makes them ideal candidates for use as inputs to CPCs. The relationships provided by Eqs. (7) and (8) indicate a maximum theoretical concentration ratio of nearly 41 – corresponding to a full power applied heat flux in excess of 47 MW/m² from a single laser module over a 0.51 cm² area – from a compact setup only 19 cm in length.

The maximum transmission efficiency of a real CPC η_{CPC} is, however, limited by several factors. Firstly, not every ray with $|\theta| \leq \theta_{\text{acc}}$ will be transmitted. Actual efficiencies for a circular profile may range from as high as 92% to as low as 67.7%, as the concentration factor increases [31]. Further, polygonal CPCs, which would be required to suit the rectangular VCSEL modules, have reduced optical efficiency compared to a circular aperture, revolved CPC [32]. The main contributions to decreases in transmission efficiencies of these systems can be attributed to:

- Sharp internal corners reflecting rays that would normally be transmitted;
- Surface scattering due to surface roughness, causing diffuse reflection and power loss;
- Fresnel reflection due to both material properties and surface roughness, leading to radiation being absorbed by the reflecting surfaces in the CPC;
- Shape inaccuracy due to machining tolerances, causing additional rays within θ_{acc} to be rejected due to a misalignment of each parabola's focal point.

These effects can be captured via the acceptance efficiency of the CPC η_{acc} , a measurement of the rays with incidence less than θ_{acc} that are accepted for an idealized shape. An estimate of the total number of internal reflections n_r can be calculated via:

$$n_r = \frac{1}{\eta_{\text{acc}}} \frac{\eta_{\text{acc}} - \eta_{\text{CPC}}(1 - \Delta\rho_e)}{\Delta\rho_e} \quad (9)$$

where changes in reflectivity ρ_e are represented using $\Delta\rho_e$. Final optical efficiency is then calculated using η_{acc} , n_r , and a one parameter estimate for surface errors due to machining that has around a 1% impact for square CPCs at VCSEL half-angle emission [32]. VCSEL module-CPC transmission efficiency is predicted for a range of reflectivities using Eq. (9) and is plotted in Fig. 8. The maximum efficiency of the system is predicted to be ~86.4%, with a rapid decrease to 63% as surface reflectivity decreases by only 5%. Decreases in transmission efficiency are fairly linear with further decreases in reflectivity.

The experimental performance of these CPCs, and the relationships between the various factors that influence their efficiency, is explored in the following sections of this paper.

3. Experimental analysis

The following section details the setup and methods used to assess the experimental performance of VCSEL-CPC systems.

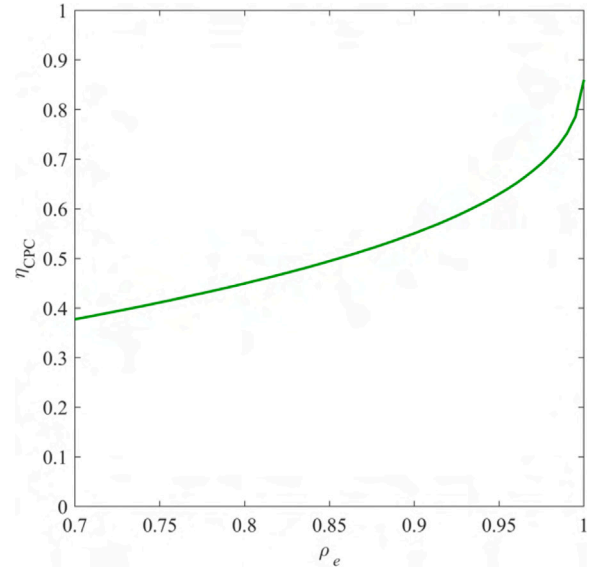


Fig. 8. VCSEL module designed CPC efficiency as a function of surface reflectivity.

Table 5

Qualitative information of the CPCs used in this study.

CPC	R_a (μm)	R_{max} (μm)	Material	Coating	C
A	0.091	0.51	Al	None	5.15
B	0.34	1.78	Al	None	5.15
C	0.99	6.08	PET	aluminum	6.55
D	1.08	8.24	PET	Gold	6.55

3.1. Setup

Two types of CPC were designed to be integrated with a single laser module to assess factors effecting the reflectivity of a CPC surface, discussed in Section 2.3, in a real environment. Two variations of each type were manufactured via 3-axis computer numerical controlled (CNC) machining to a tolerance level of ± 0.00508 mm. Parametric information for each is given in Table 5, with dimensions shown in Fig. 9.

CPCs A/B were manufactured out of aluminum and designed to assess the impacts of varied surface roughnesses. They had bare surfaces with decreasing average surface roughnesses R_a resulting from medium and fine hand polishing. CPCs C/D were designed to facilitate an investigation on the impacts of surface coating, and were manufactured out of polyethylene terephthalate (PET), with internal surfaces coated with thin layers of gold and aluminum. CPCs C/D were both finished to the same R_a of near 1 μm , representing the lowest R_a possible for a PET component. Both coatings were deposited via closed field unbalanced magnetron sputter ion plating to ensure a hard and durable coating on the PET substrate. Coating thicknesses were 400 nm, which was guaranteed by the coating specialists to ensure the total reflectance of the coating. Both were deposited onto a base 200 nm thick bond layer of chromium.

The three R_a values included in this study represent affordable and readily achievable finishing options for a CPC of any shape. Similarly, gold and aluminum coatings were chosen to provide both an efficiency and a cost comparison, as both have theoretically high reflectivity characteristic in the near-infrared [33] but vary significantly in additional cost (e.g. an as-machined, uncoated aluminum CPC is significantly less cost intensive than one that has a gold coating applied). However, as polished aluminum is prone to environmental degradation [34], a secondary focus of this investigation was to quantify any knock-down effects on its theoretical reflectivity. The coated CPCs are shown in Fig. 10.

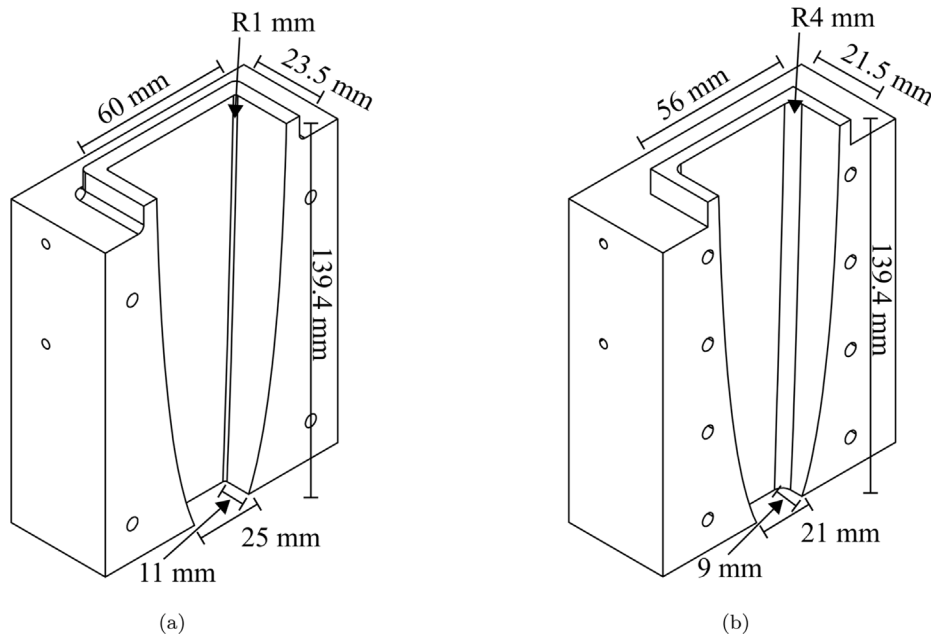


Fig. 9. Key dimensions of CPCs A/B (a) and C/D (b).

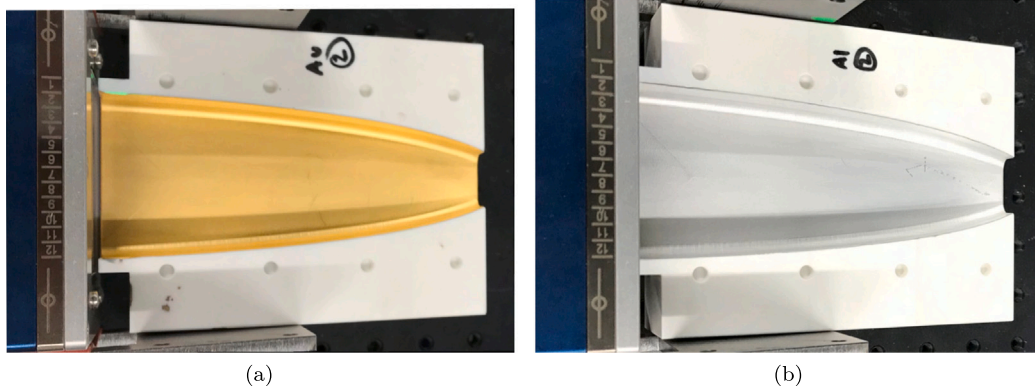


Fig. 10. Gold (a) and aluminum (b) coated, PET body CPC geometries shown co-mounted with a VCSEL module.

The VCSEL modules and CPCs were co-mounted to minimize losses arising from misalignment of the system. Steel targets were placed at the exit aperture of the CPC, and were manufactured out of 0.9 mm thick sheets of 304 grade stainless steel (UNS S30400). Instrumentation guide markings were laser etched at a depth of 0.002 mm on the back of the target face during the manufacturing process. Each target surface was coated with a layer of high-emissivity paint⁸ to maximize the absorption of the laser into the target. The absorption value was calibrated, and is detailed in Section 4.1. Both the calibration and CPC experimental setups are shown in Fig. 11.

3.2. Methodology

A combination of numerical simulation methods were used to create a computational representation of the experimental system. These processes are detailed in subsequent subsections, along with an analysis of the uncertainties present in the combined numerical-experimental approach taken in this study. Experimental tests were designed such that the laser was active for a combined short duration and power level

capable of generated measured surface temperatures on the steel target of at least 400 °C. This served two purposes:

1. Short transients limited in-plane conduction within the target and made the effects of re-radiation and natural convection negligible relative to the applied laser power.
2. Surface temperatures above 400 °C allowed for the use of the facility's ratio pyrometers, which enabled high accuracy and emissivity independent surface temperature measurements. Pyrometers capture the maximum temperature within a target area.

For each set of tests the pyrometer was aimed such that the measurement area, marked by the green laser circle seen on the target in Fig. 11, contained the maximum generated temperature. The location of this area was informed by the computational modeling and infrared camera used during testing. The IR camera was used for diagnostic purposes only to avoid introducing any emissivity related errors to the results, as maximum temperature values were already recorded by an emissivity-independent pyrometer.

The maximum temperatures captured by the pyrometer and predicted numerically result from laser pulses at the same power setting, thus any differences in temperature between the two are the direct

⁸ Aremco HiE-Coat™ 840-CM; <https://www.aremco.com/high-emissivity-coatings/>.

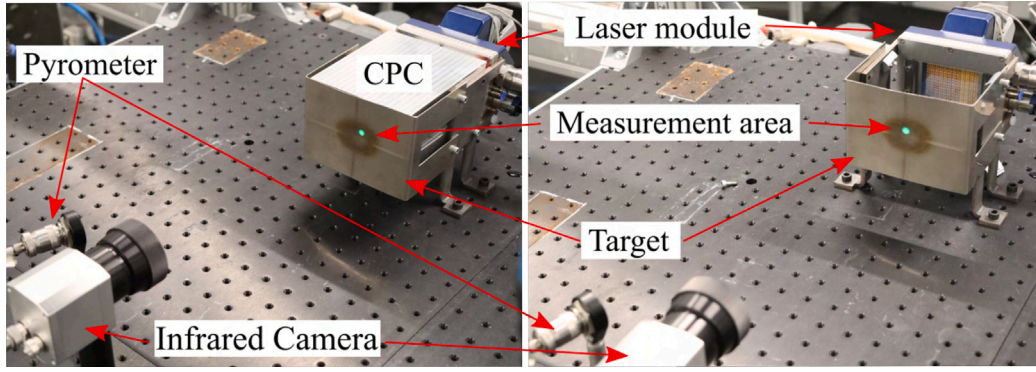


Fig. 11. Diagrams showing the CPC (left), and absorption calibration (right) experimental setups.

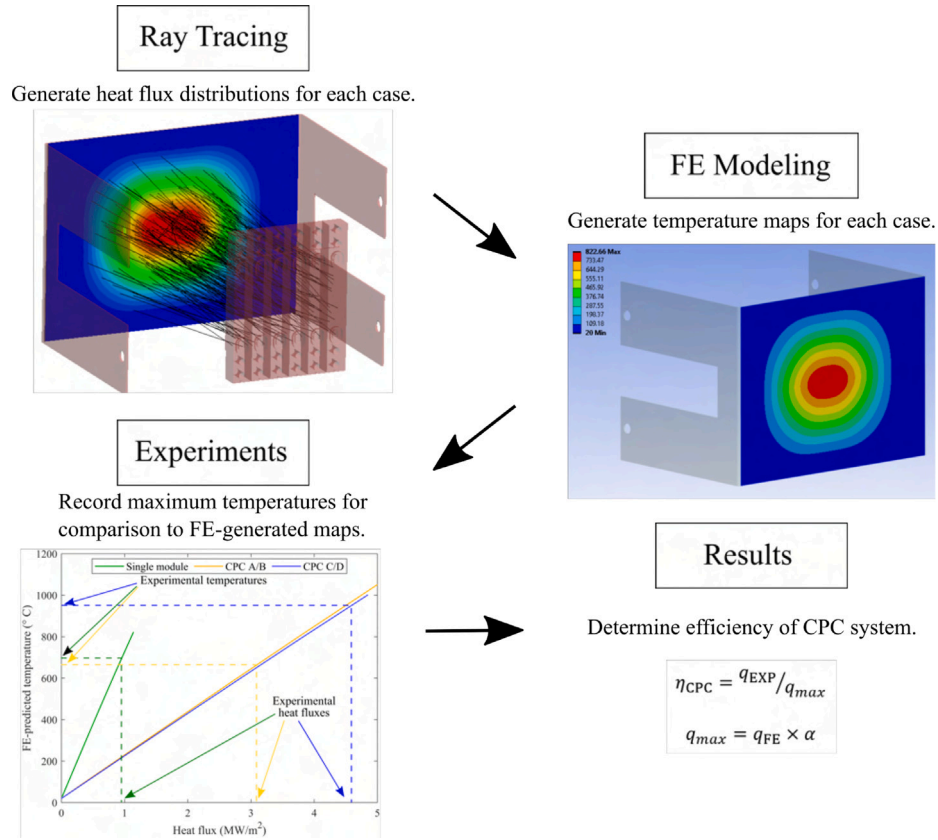


Fig. 12. The combined numerical-experimental methodology used in this study to determine coating absorption and CPC efficiency.

result of losses in the coating and CPC. This enabled a comparison of experimental temperatures to numerical ones, and the determination of both coating laser absorption and optical CPC transmission efficiencies η_{CPC} through the following ratios:

$$\eta_{CPC} = \frac{q_{exp}}{q_{max}} \quad (10)$$

$$q_{max} = \alpha q_{FE} \quad (11)$$

where the heat flux terms are defined as follows:

- q_{exp} is the experimental heat flux at the surface of the target and corresponds to the experimental temperature measured during each laser pulse and is determined using the FE-generated temperature maps for each setup;
- q_{FE} is the ray-tracing-generated maximum incident heat flux, which assumes both perfect absorption ($\alpha = 1$) and reflectance ($\rho_e = 1$) of any CPC system;

- q_{max} is the maximum possible heat flux transmitted into the target surface, and is the ray tracing generated profile scaled by the absorption of the laser.

This overall process is summarized in Fig. 12.

3.2.1. Computational analyses

Ray tracing and finite element (FE) analyses were used to model and predict the temperature distributions generated during both the baseline and CPC experiments. For each case, ray tracing was performed in LightTools® using the VCSEL parameters determined in Section 2.2 to produce the experimental heat flux distributions incident on the target. These assumed a 2.4 kW laser module at full power for each testing configuration. Interior curved surfaces of the CPC were modeled as simple mirrors ($\rho_e = 1$) and the target surface with perfect absorption ($\alpha = 1$). A total of 10 million rays were simulated alongside a target surface mesh with 0.2 mm by 0.2 mm resolution. An example of

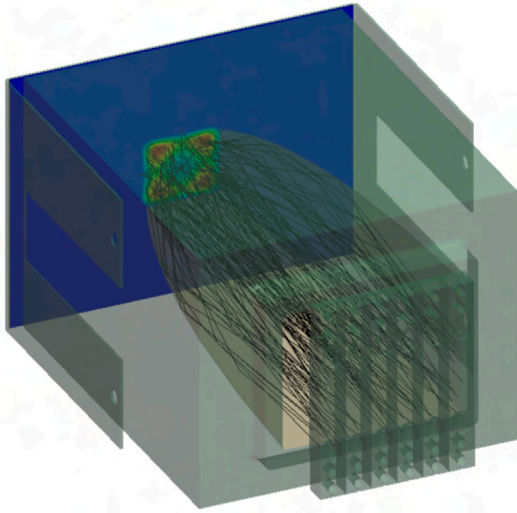


Fig. 13. Simulated ray paths for CPCs C/D.

the resulting intensity patterns, and simulated ray paths, is shown in Fig. 13.

These heat flux profiles, shown in Fig. 14, were then imported to ANSYS Mechanical 2020 R1 as the driving boundary condition in transient thermal simulations. Each was scaled to the experimental power settings determined to meet the conditions in the previous section, and provided a prediction of the maximum experimental temperature that would be seen on the target if both the transmission of the laser through the CPC and its absorption into the target were perfect. Environmental temperature was fixed to 20 °C and additional boundary conditions were applied to the steel target: radiation boundary conditions were added to the painted target surface and uncoated steel surfaces with representative emissivity values of 0.9 and 0.35, respectively, and a natural convection boundary condition was applied to all surfaces with a convection coefficient of 5 W/m²K. The variation of predicted temperatures to changes in these values is captured in the uncertainty analysis detailed in the next section.

Time and mesh sensitivity studies were done to ensure the independence of the results generated from these analyses. The mesh size on the face where the surface where the laser is incident was fixed to 0.2 mm by 0.2 mm to prevent interpolation errors when importing the heat flux profile. The sensitivity analyses fixed a characteristic mesh size of 0.5 mm elsewhere, for a total of 197676 elements, and simulation time steps of 27.5 ms.

Predicted temperatures at the end of each laser pulse are plotted in Fig. 15 against a range of maximum heat fluxes resulting from changes in transmitted and absorbed laser power. CPCs A and B have slightly increased maximum temperatures compared to CPCs C and D due to the higher heat flux peaks seen in the distribution relative to the overall concentration ratio, and results from the smaller fillet radius at the intersection of the curved parabolic surfaces. The maximum temperature points plotted correspond to cases with perfect absorption and CPC transmission. These temperature maps were then used with temperature measurements taken at each test condition to find the corresponding experimental heat flux q_{exp} incident on the target.

3.2.2. Uncertainty analysis

The combined small perturbation and finite difference approach of Taylor [35] was used to estimate the uncertainties present in the

Table 6

Tabulation of uncertainties present when calibrating VCSEL emission absorption.

Parameter	Typ. value	Uncert.	$(\delta h_c / \delta \chi) \Delta \chi_i / h_c$
<i>Experimental</i>			
Pyrometer _{meas}	727.46 °C	5.61 °C	0.0083
Pyrometer _{t,sample}	2.75 s	0.02 s	0.0089
DAQ _{gain}	8.87 mA	0.067 mA	8.96×10^{-4}
DAQ _{range}	22 mA	0.0088 mA	6.7×10^{-3}
<i>Computational</i>			
Emissivity	0.9	0.1	0.0021
Natural convection	5 W/m ² K	5 W/m ² K	0.0034
Environment	20 °C	2 °C	-3.17×10^{-5}
Total uncertainty			$\pm 1.39\%$

Table 7

Baseline absorption results, both before and after testing.

	q_{FE} (MW/m ²)	T_{FE} (°C)	T_{exp} (°C)	q_{exp} (MW/m ²)	α
Pre	1.14	823.3	722.3	0.99	0.870
Post			727.5	1.0	0.876

system. The total uncertainty percentage U_{tot} in resulting from this analysis are calculated using a root-sum-square method:

$$U_{\text{tot}} = \sqrt{\sum_{i=1}^N \left[\left(\frac{\delta h_c}{\delta \chi_i} \right) \frac{\Delta \chi_i}{h_c} \right]^2} \quad (12)$$

The change in each variable h_c relative to the source of the uncertainty is given by the partial derivative $\delta h_c / \delta \chi_i$ while $\Delta \chi$ is the magnitude of each uncertainty and h_c is the most likely (calculated) value for each case.

The calculation of the VCSEL emission absorption is provided as an example of this approach, where the experimental uncertainties are located in the pyrometer (measurement, sample rate) and data acquisition system (gain, range), with computational uncertainties located in the values of the individual thermal boundary conditions (emissivity, natural convection, environment temperature). The contributions of each of these to the overall uncertainty are presented in Table 6. Time response uncertainties for the facility's pyrometers were not considered given their characteristic 1 ms response time being much less than the test duration.

4. Experimental results and discussion

4.1. Absorption baseline

VCSEL absorption was calibrated using a 2.75 s, 2.4 kW laser pulse. The target was approximately 110 mm from the module surface and mounted in the same jig as the CPCs in subsequent analyses. Tests were carried out both before and after these CPC tests to check for any changes in paint absorption.

Results of this analysis are given in Table 7. There was little change between the start and end of testing indicating a high level of survivability of the coating even at elevated heat fluxes. The final absorption value for the coating carried forward to subsequent analyses was calculated as the average between the two cases for a value of 0.873 ± 0.012 ($\pm 1.39\%$).

4.2. Surface coating

Surface coating transmission efficiencies were calculated using temperatures measured from a 1 s, 1.2 kW laser pulse. FE-predicted temperatures after a 1 s second pulse, alongside a demonstrative IR camera-captured temperature distribution at the same time, are shown in

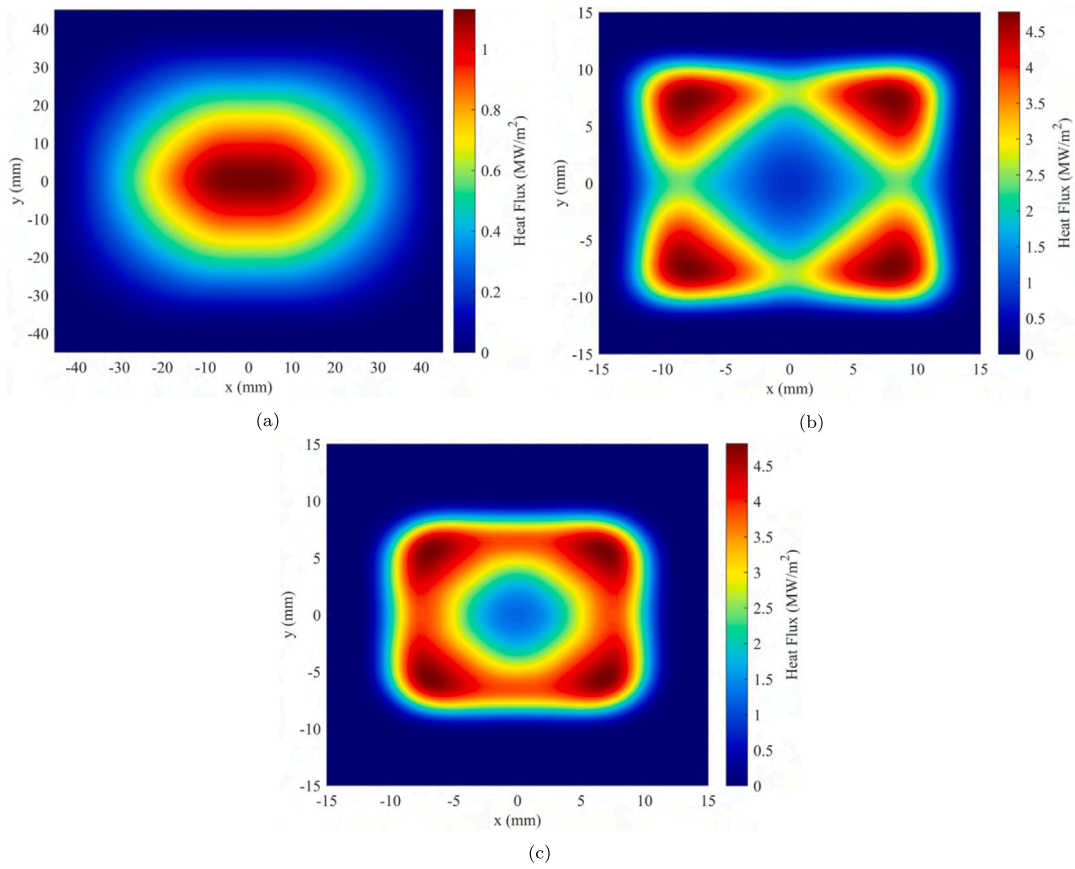


Fig. 14. Ray-tracing-generated heat flux profiles for the absorption calibration (a), CPC A/B (b), and CPC C/D (c) experimental setups.

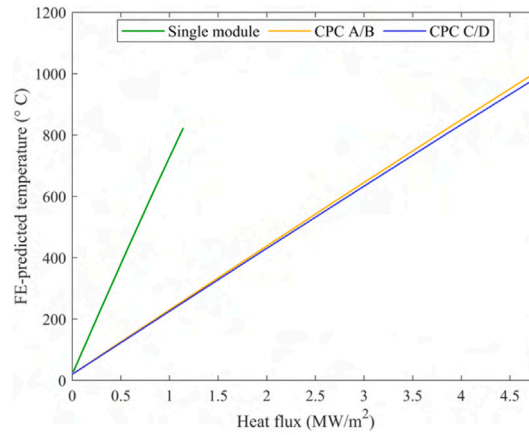


Fig. 15. FE predicted maximum temperatures for the absorption baseline and CPC A/B and C/D experimental setups.

Fig. 16.⁹ Experimental and computational maximum temperatures are compared in Table 8.

The gold coating outperformed the aluminum case, providing a base efficiency approximately 22% higher than the aluminum case. While this is not unexpected, this is higher than would be the case

⁹ The non-symmetric temperature profile in the IR-camera image – the peak temperature on the left side is approximately 50 °C lower than the right – is likely the result of surface emissivity inconsistencies (e.g. oxidation due to high temperature) on the steel target. As the camera was used as a solely as a diagnostic aid the camera setup was not calibrated. Similarly, given the emissivity-independence of the pyrometer measurements above a target temperature, the quality of the back surface of the target was not controlled.

Table 8

Results of the CPC surface coating analysis.

Coating	q_{FE} (MW/m ²)	T_{FE} (°C)	T_{exp} (°C)	q_{exp} (MW/m ²)	η_{CPC} (%)
Au	4.8	1001.7	588.5	2.8	66.8
Al			490.4	2.3	54.9

purely based on reflectivity differences between the two materials and indicates further interactions between the laser and the aluminum coating. This is perhaps related to the previously mentioned environmental degradation, whereby a stable aluminum oxide layer with low reflectivity forms on the surface of the CPC [34]. Gold is therefore the

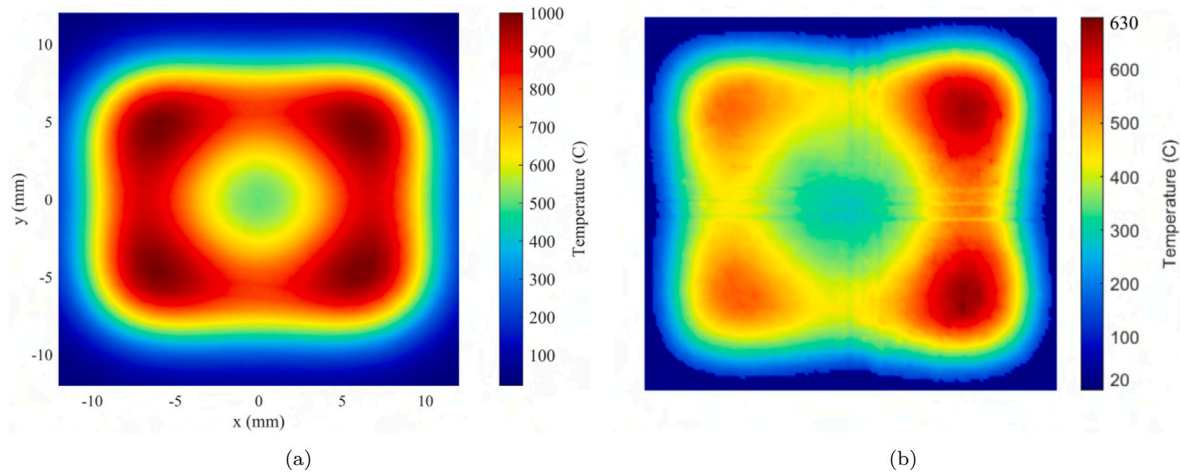


Fig. 16. FE-predicted temperature distribution for CPC C/D (a) alongside an experimental, IR-camera captured temperature profile (b).

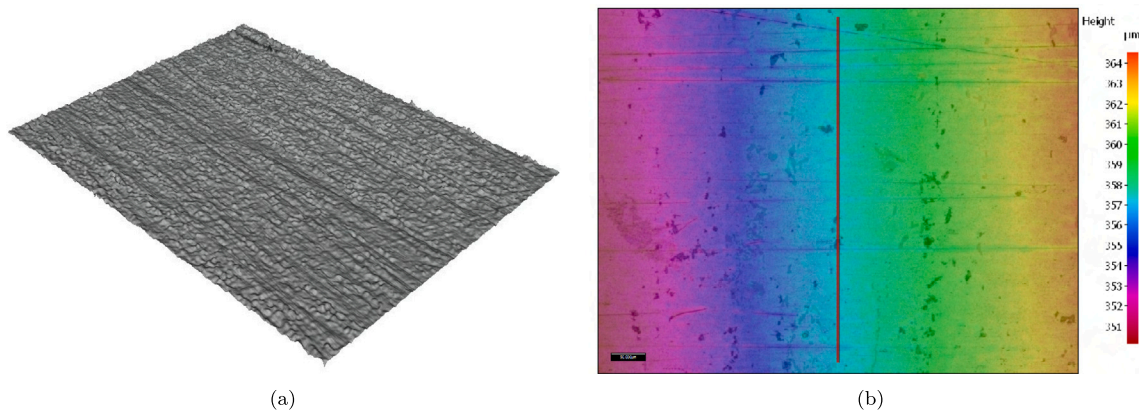


Fig. 17. Alicona generated 3-D render of a CPC surface roughness map (a) and line data sample location shown against the relative curvature of the CPC (b).

preferable coating if maximizing transmission efficiency is a primary aim, particularly when the highest heat fluxes are required in an experimental test. This has to be weighed against the total cost of the experimental setup, as the deposition of even a thin layer of gold to an aluminum component can represent a significant portion, or even the majority, of the cost of the experimental system.

4.3. Surface roughness

Rougher surfaces scatter more of the incoming light, making surface roughness a key concern in optical systems. This can be completely avoided by ensuring finished surfaces have R_a values that are much less than the wavelength of the incoming light [36]. Achieving this requires specialist equipment and finishing techniques (e.g. high precision mechanical lapping equipment or chemical etching [37]) that in turn incur increases in costs and production times. It was determined the non-standard shape of the internal parabolic surfaces of the square cross-section CPCs investigated in this study were incompatible with these processes, leaving surface roughness down to the nanometer range or lower out of reach. This study therefore aims to determine if a threshold exists whereby reasonable system efficiency is maintained for standard machining and finishing techniques. The values of roughness presented here represent three levels that are still easily and affordably attained via mechanical finishing and polishing following standard manufacturing processes [38].

Surface roughness maps were optically measured using an Alicona G4 Infinite Focus near the inlet aperture of each concentrator. This location was deemed sufficiently representative of the full surface given

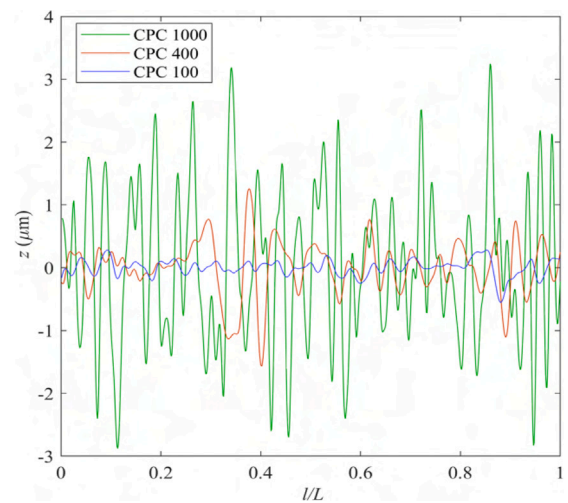


Fig. 18. Line data showing the surface height z variation along a normalized section of each CPC analyzed.

the same finishing procedure was used across the entire CPC. The resulting roughness map was then sampled across three discrete lines. Representative sample profiles for each CPC is shown in Fig. 18. These lines were taken perpendicular to the main curvature of the body (“across” the CPC). Roughness data measured parallel to the curvature

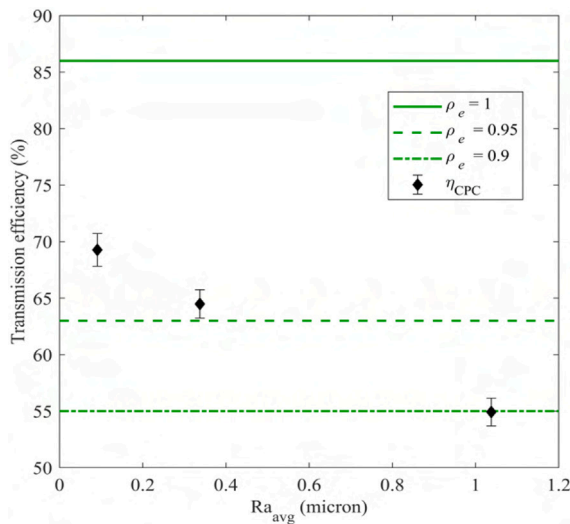


Fig. 19. VCSL power transmission efficiency as a function of average surface roughness, for CPCs with untreated aluminum surfaces.

Table 9
Results of the surface roughness analysis.

CPC	R_a (μm)	q_{FE} (MW/m^2)	T_{FE} ($^{\circ}\text{C}$)	T_{exp} ($^{\circ}\text{C}$)	q_{exp} (MW/m^2)	η_{CPC} (%)
A	0.091	4.8	1051.5	629.6	2.9	69.2
B	0.34	4.8	1051.5	583.3	2.7	64.4
C	0.99	4.8	1001.7	490.4	2.3	54.9

of the body (“down” the CPC towards the exit aperture) are skewed by the fractional increase in height from one end of the measured area to the other. This effect is shown in Fig. 17 alongside a 3-D render of the surface. The resulting statistical data from each of the three line measurements was averaged for each CPC. The resulting averaged R_a and maximum roughness values R_{max} are shown in Table 5.

The effects of surface roughness on transmission efficiency were investigated using a 1 s, 1.5 kW laser pulse. Resulting experimental temperatures are compared to computational data in Table 9.

There is a sustained increase in transmission efficiency with decreasing surface roughness: η_{CPC} increases by 26.1% from 54.9% ($\pm 1.22\%$) to 69.2% ($\pm 1.44\%$) as R_a decreases by an order of magnitude. This is shown in Fig. 19 and relates to a comparable change in surface reflectivity from 0.9 to 0.975. The low overall performance of the system in these results is limited by the aluminum coating, which was previously shown in this study to have low reflectivity. Extrapolating the effects on increased reflectivity of a gold coating over an aluminum as described in Section 4.2, η_{CPC} would increase to $\sim 84.4\%$. This represents approximately 98% of the maximum transmission efficiency of the system and indicates a high level of performance at an easily achievable surface roughness.

5. Future work

While the experimental work here focused on uncooled targets, the modular nature of OLAHF allows for the possibility of a wide-range of studies to be conducted on actively cooled components in a variety of environments. These could range from CFD validation experiments to accelerated component lifing analyses. Either would be readily achieved using either the of the available air or water supplies, or with an alternative cooling medium (e.g. supercritical carbon dioxide) through the installation of new supporting infrastructure.

5.1. Upgraded CPC capabilities

Two larger CPCs, integrating larger numbers of laser modules, have been designed and used in thermal fatigue testing of aerospace and fusion components: one for use with the four, 2.4 kW modules (9.6 kW input), and one for use with the three, 4.8 kW modules (14.4 kW input). They have concentration ratios of approximately 15 and 30 with output areas of $35 \times 35 \text{ mm}$ and $48 \times 20 \text{ mm}$, respectively. These CPCs, and their corresponding full-power applied intensity profiles are shown in Fig. 20.

Both were manufactured out of aluminum (UNS A96062), have internal surfaces polished to $R_a \leq 200 \mu\text{m}$, and are plated in 50 nm of NiCr and 400 nm gold. Both are fully water-cooled locally at the exit apertures to prevent both damage and distortion of the CPC arising from radiation from the high-temperature test targets. The brackets that mount the modules in each CPC system are also water-cooled and are polished and coated to the same degree as the CPC. This serves two purposes:

1. Surface finishing of this level serves to deflect thermal radiation, thereby keeping the laser modules safe from elevated temperatures.
2. This has been determined to increase η_{CPC} by 18%–54% as the rejected rays are directed back towards the exit aperture.

5.2. Addressing limitations

Ensuring consistent, and known, laser absorption into target test pieces and applying even heat flux distributions at the exit apertures of CPCs remain two significant limitations of the facility detailed in this paper. The coating detailed in Section 4.1 has proven durable when used on metallic components, and work is ongoing towards the deployment of a coating suitable for ceramic materials. Testing has nevertheless been undertaken with uncoated components after determining the related characteristic absorption value, with the understanding that this often limits the available level of applied power.

The non-uniformity present in the heat flux distributions seen at the exit of CPC apertures has prompted proposals for optimization studies focused on reducing it. The nature of CPC design, and the level of control available from the laser modules, are two factors currently being investigated.

6. Conclusions

This paper has presented the work done to date developing and commissioning OLAHF, a new high heat flux test facility. The combination of the facility’s seven VCSL modules – totaling 24 kW of total power – and a range of water, air and instrumentation infrastructure allows for a wide range of component-scale testing that is unique in the UK. In particular, the lasers system at OLAHF is one of few locations capable of high heat flux testing non-metallic components at thermal loads characteristic of the aerospace or fusion sectors.

Following the validation of a computational model of the facility’s laser modules, a study was conducted into using them as inputs to CPCs thereby significantly increasing applied heat flux capabilities. The influences of surface roughness and coating on CPC transmission efficiency were experimentally investigated using four CPCs and a steel target coated with a paint that was determined to absorb 87.3% of the applied laser. Gold surfaces were found to have 22% higher transmission efficiency than aluminum ones for CPCs with similar surface roughnesses. Further, decreasing average surface roughness from $1 \mu\text{m}$ to $0.1 \mu\text{m}$ resulted in an increase in η_{CPC} of 226.1%. These results indicate a VCSL-CPC system with 98% of the maximum theoretical transmission efficiency ($\eta_{CPC,max} = 86.4\%$) when gold coatings and standard surface finishes are employed.

Future work involving two larger CPCs, which apply peak experimental heat fluxes of 7.5 and 34 MW/m^2 through the use of larger

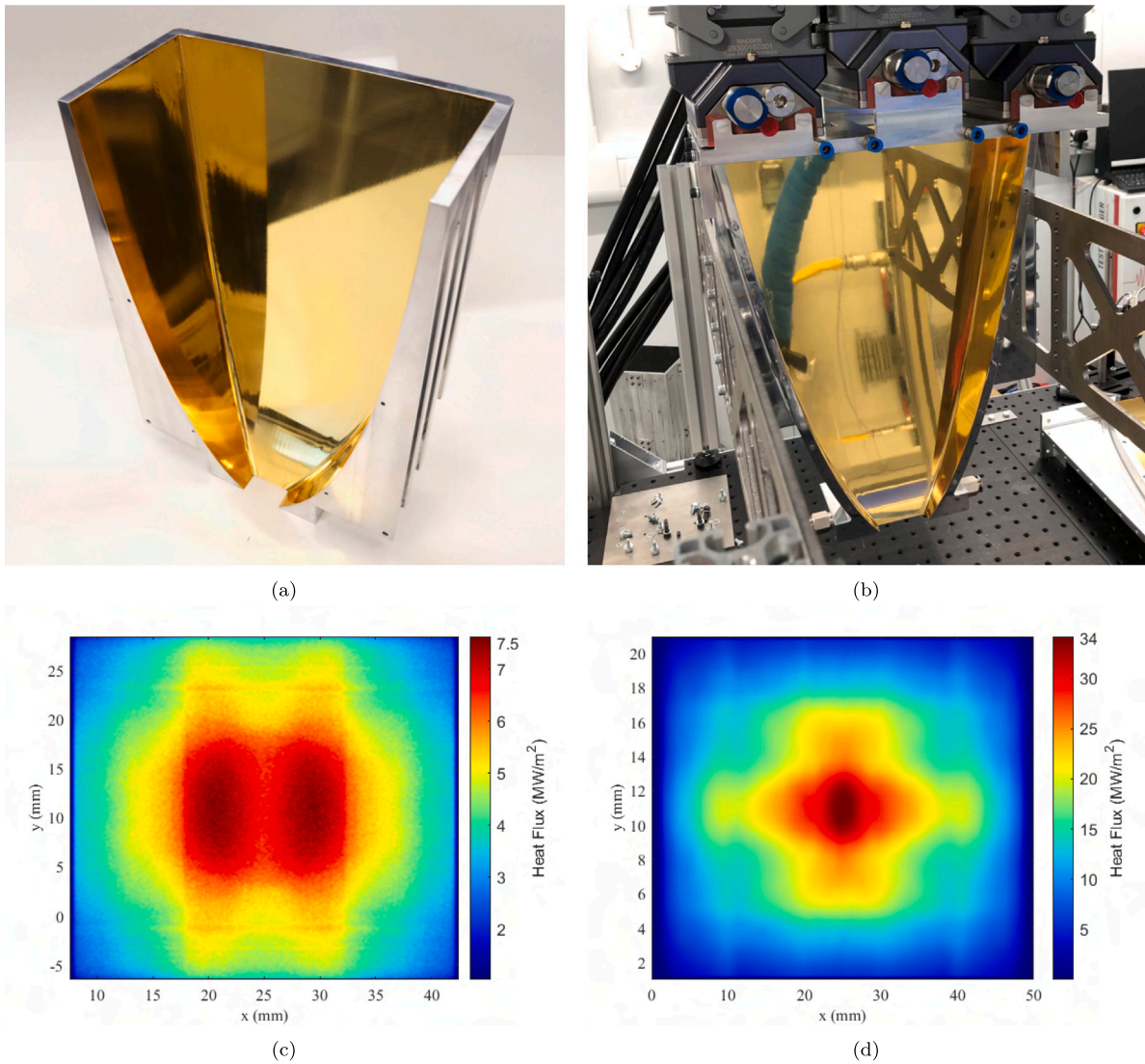


Fig. 20. Cross sectional views and full-power applied heat flux profiles of the CPCs that integrate the four, 2.4 kW (a) (c) and 3, 4.8 kW (b) (d) laser modules.

numbers of laser modules, is planned to extend the testing potential of OLAHF while work is ongoing to homogenize CPC-applied heat fluxes and maximize its absorption into target components.

CRediT authorship contribution statement

Zachary Jackson: Writing – review & editing, Writing – original draft, Visualization, Validation, Project administration, Methodology, Investigation, Funding acquisition, Formal analysis, Data curation, Conceptualization. **Alexander Bebb:** Writing – review & editing, Writing – Section 2.3 draft. **Peter Ireland:** Writing – review & editing, Supervision, Funding acquisition. **Jack Nicholas:** Methodology, Conceptualization.

Declaration of competing interest

The authors declare the following financial interests/personal relationships which may be considered as potential competing interests: Zachary Jackson reports financial support was provided by Innovate UK. Zachary Jackson reports financial support was provided by Tokamak Energy Ltd. Zachary Jackson reports a relationship with Rolls-Royce plc that includes: funding grants. If there are other authors, they declare that they have no known competing financial interests or personal relationships that could have appeared to influence the work reported in this paper.

Data availability

Data will be made available on request.

Acknowledgments

This work was supported by InnovateUK through the CEMTEC program under Grant reference No 113160 and Tokamak Energy Ltd as a part of the BEIS AMR Phase 2 project. The support of David Chapman, Clive Siviour, Nick Hawkins and the technicians at the Oxford Thermofluids Institute in developing this facility is greatly acknowledged.

Appendix. The 1-D heat equation

The steady state heat equation in one dimension is $k \frac{d^2 T}{dx^2} = 0$ (13)

which when solved for the boundary conditions in Section 1.1 yields the general solution

$$T(x) = q \left(\frac{1}{h} (1 + \text{Bi}) - \frac{x}{k} \right) + T_{ci} \quad (14)$$

Solving for $\Delta T = T(x=0) - T(x=L)$ gives

$$\Delta T = \frac{qL}{k} \quad (15)$$

$$T(x=0) = T_{max} = \left(\frac{1 + Bi}{Bi} \right) \Delta T + T_{ci} \quad (16)$$

References

- [1] G. Moreno, Power Electronics Thermal Management, Technical Report, National Renewable Energy Laboratory, 2020.
- [2] T. Hammer, et al., Natural gas oxy-fuel cycles-Part 2: Heat transfer analysis of a gas turbine, *Energy Procedia* 1 (2009) 557–564, <http://dx.doi.org/10.1016/j.egypro.2009.01.074>.
- [3] D. Isakeit, et al., The Atmospheric Reentry Demonstrator, Technical Report, European Space Agency, 1998.
- [4] E. Josyula, et al., Hypersonic nonequilibrium flow computations using the roe flux-difference split scheme, *AIAA J.* 31 (1993) 812–813, <http://dx.doi.org/10.2514/3.11687>.
- [5] J.H. You, et al., High-heat-flux technologies for the European demo divertor targets: State-of-the-art and a review of the latest testing campaign, *J. Nucl. Mater.* 544 (2021) <http://dx.doi.org/10.1016/j.jnucmat.2020.152670>.
- [6] C. Skamniotis, A.C.F. Cocks, Analytical shakedown, ratchetting and creep solutions for idealized twin-wall blade components subjected to cyclic thermal and centrifugal loading, *Eur. J. Mech. A Solids* 95 (2022) 104652, <http://dx.doi.org/10.1016/j.euromechsol.2022.104652>.
- [7] C. Skamniotis, A.C.F. Cocks, Ratchetting and creep failure in twin-wall turbine blades experiencing severe thermal and centrifugal loading, *J. Appl. Mech.* 89 (9) (2022).
- [8] T. Barrett, et al., Enhancing the DEMO divertor target by interlayer engineering, *Fusion Eng. Des.* 98–99 (2015) 1216–1220, <http://dx.doi.org/10.1016/j.fusengdes.2015.03.031>, Proceedings of the 28th Symposium On Fusion Technology (SOFT-28).
- [9] P. Majerus, et al., The new electron beam test facility JUDITH II for high heat flux experiments on plasma facing components, *Fusion Eng. Des.* 75–79 (2005) 365–369, <http://dx.doi.org/10.1016/j.fusengdes.2005.06.058>.
- [10] C. Linsmeier, B. Unterberg, J. Coenen, R. Doerner, H. Greuner, A. Kreter, J. Linke, H. Maier, Material testing facilities and programs for plasma-facing component testing, *Nucl. Fusion* 57 (9) (2017) 092012, <http://dx.doi.org/10.1088/1741-4326/aa4feb>.
- [11] I. Bobin-Vastra, et al., Activity of the European high heat flux test facility: FE200, *Fusion Eng. Des.* 75–79 (2005) 357–363, <http://dx.doi.org/10.1016/j.fusengdes.2005.08.023>.
- [12] J. McDonald, T. Lutz, D. Youchison, F. Bauer, K. Troncoso, R. Nygren, The sandia plasma materials test facility in 2007, *Fusion Eng. Des.* 83 (7) (2008) 1087–1091, <http://dx.doi.org/10.1016/j.fusengdes.2008.06.062>.
- [13] Y. Hamaji, et al., ACT2: A high heat flux test facility using electron beam for fusion application, *Plasma Fusion Res.* 11 (2016) 2–5, <http://dx.doi.org/10.1585/pfr.11.2405089>.
- [14] T. Hirai, K. Ezato, P. Majerus, ITER relevant high heat flux testing on plasma facing surfaces, *Plasma Trans.* 46 (3) (2005) 412–424, <http://dx.doi.org/10.2320/matertrans.46.412>.
- [15] S.-K. Kim, et al., Performance qualification for high heat load components of fusion reactor in KAERI, in: Transactions of the Korean Nuclear Society Autumn Meeting, 2017.
- [16] Y. Lian, et al., Manufacturing and high heat flux testing of brazed flat-type W/CuCrZr plasma facing components, *Plasma Sci. Technol.* 18 (2) (2016) 184, <http://dx.doi.org/10.1088/1009-0630/18/2/15>.
- [17] J. Prokupek, et al., HELCZA high heat flux test facility for testing ITER EU first wall components, *Fusion Eng. Des.* 124 (2017) 187–190, <http://dx.doi.org/10.1016/j.fusengdes.2017.03.059>.
- [18] H. Greuner, et al., High heat flux facility GLADIS: Operational characteristics and results of W7-X pre-series target tests, *J. Nucl. Mater.* 367–370 B (2007) 1444–1448, <http://dx.doi.org/10.1016/j.jnucmat.2007.04.004>.
- [19] Q. Li, et al., 100 kW electron-beam high heat flux test facility for testing EAST and CFETR divertor components, *Fusion Eng. Des.* 183 (2022) <http://dx.doi.org/10.1016/j.fusengdes.2022.113276>.
- [20] A.S. Sabau, et al., A 6 MW/m² high heat flux testing facility of irradiated materials using infrared plasma-arc lamps, *Fusion Sci. Technol.* 75 (7) (2019) 690–701, <http://dx.doi.org/10.1080/15361055.2019.1623571>.
- [21] Culham Centre for Fusion Energy (CCFE), CHIMERA, 2023, URL: <https://ccfe.ukaea.uk/divisions/fusion-technology/chimera/>. (Online, accessed 15 October 2020).
- [22] D. Hancock, et al., Testing Advanced Divertor Concepts for Fusion Power Plants Using a Small High Heat Flux Facility, Technical Report UKAEA-CCFE-PR(23)183, Culham Centre for Fusion Energy (CCFE), 2023.
- [23] Technische Universität Dresden, Mini specimen test rig, 2023, URL: <https://tu-dresden.de/ing/maschinenwesen/iet/tea/die-arbeitsgruppe/technische-ausstattung/versuchsanlagen/mini-proben-pruefsystem>. (Online, accessed 15 October 2020).
- [24] E. Chang, T. Hermann, System study of an integrated facility with arc-jet and expansion tube for hypervelocity testing with ablating spacecraft models, in: HiSST: 3rd International Conference on High-Speed Vehicle Science Technology, 2024.
- [25] National Composites Centre, Ceramic matrix composites, 2023, URL: <https://www.nccuk.com/what-we-do/technologies/ceramic-matrix-composites/>. (Online; accessed 13 January 2023).
- [26] C. Skamniotis, et al., Multiscale analysis of thermomechanical stresses in double wall transpiration cooling systems for gas turbine blades, *Int. J. Mech. Sci.* 207 (2021) 106657, <http://dx.doi.org/10.1016/j.ijmecsci.2021.106657>.
- [27] T. Weiler, et al., Optical modelling of VCSEL-assisted thermoplastic tape placement, in: 17th European Conference on Composite Materials, 2016.
- [28] Philips GmbH Photonics Aachen, Intensity patterns of PPM412 type VCSEL laser modules, 2017.
- [29] R. Winston, et al., Nonimaging Optics, Elsevier, 2005, <http://dx.doi.org/10.1016/B978-0-12-759751-5.X5000-3>.
- [30] A. Rabl, Optical and Thermal Properties of Compound Parabolic Concentrators, Technical Report, Pergamon Press, 1976, pp. 497–511.
- [31] S. Darbe, Optics for High-Efficiency Full Spectrum Photovoltaics (Ph.D. thesis), California Institute of Technology, 2017.
- [32] T. Cooper, et al., Performance of compound parabolic concentrators with polygonal apertures, *Sol. Energy* 95 (2013) 308–318, <http://dx.doi.org/10.1016/j.solener.2013.06.023>.
- [33] Fluke Process Instruments, Emissivity - Metals, 2023, URL: <https://www.flukeprocessinstruments.com/en-us/service-and-support/knowledge-center/infrared-technology/emissivity-metals>. (Online; accessed 4 March 2022).
- [34] LBP Optics, Reflectivity of aluminium - UV, visible and infrared, 2014, URL: <https://laserbeamproducts.wordpress.com/2014/06/19/reflectivity-of-aluminium-uv-visible-and-infrared/>. (Online; accessed 21 June 2021).
- [35] J. Taylor, An Introduction to Error Analysis, second ed., University Science Books, 1997.
- [36] H. Bennett, J. Porteus, Relation between surface roughness and specular reflectance at normal incidence, *J. Opt. Soc. Am.* 51 (1961).
- [37] J. Nelson, S. Iles, Creating sub angstrom surfaces on planar and spherical substrates, in: Proceedings Volume 11175 Optifab 2019, SPIE, 2019, p. 1, <http://dx.doi.org/10.1117/12.2536689>.
- [38] ISO Finishing, Surface roughness in manufacturing, 2023, URL: <https://isofinishing.com/surface-roughness-in-manufacturing/>. (Online; accessed 20 June 2021).